RESEARCH ARTICLE

ESPL WILEY

Imaging mass-wasting sliding surfaces within complex glacial deposits along coastal cliffs using geophysics

Simon Blondel[1,2] | Sebastian Uhlemann[3,4] | Cornelia Inauen[4] |
Arnaud Watlet[4] | Hansruedi Maurer[5] | Colm Jordan[4] | Jonathan Lee[4] |
Jonathan Chambers[4]

[1]National Institute of Oceanography and Applied Geophysics (OGS), Trieste, Italy

[2]Department of Mathematics and Geosciences, University of Trieste, Trieste, Italy

[3]Earth and Environmental Sciences Area, Lawrence Berkeley National Laboratory, Berkeley, CA, USA

[4]British Geological Survey, Nottingham, UK

[5]Institute of Geophysics, ETH Zurich, Zurich, Switzerland

Correspondence
Simon Blondel, National Institute of Oceanography and Applied Geophysics (OGS), Trieste 34151, Italy.
Email: simon.blondel2@gmail.com

Abstract

This study presents a multidisciplinary survey combining geological fieldwork and geophysical data to better constrain the parameters influencing the morphology and behaviour of a retreating coastal cliff. Erosion rates are spatially highly variable and hard to predict because of the manifold parameters acting on them. Among these parameters, rock resistance exerts a paramount influence on cliff retreat. Characterizing the rock resistance distribution along a coastal region requires the mapping of several key subsurface properties including the bulk lithology, faulting, fracturing, or weathering. This is a difficult and expensive task because of the high spatial variability of these factors linked to the spatial complexity of the geology. Geophysical methods can be used to tackle this challenge by quickly providing the 3D visualization and distribution of these parameters within the subsurface. A fast-eroding portion of the Norfolk coast (UK) at West Runton is investigated using a multidisciplinary approach, combining ground-penetrating radar, electrical resistivity tomography (ERT), cone penetration tests, and outcrop studies. The results allowed us to build a 3D geological and geophysical model of a highly complex area of glacial geology. It forms part of a relict glaciotectonic thrust-tip moraine and sand basin sequence. The surfaces interpreted on radar data are associated with strong resistivity contrasts on the ERT data. These contrasts have been attributed to petrophysical variations between the lithological units. The base of the sand basin is marked by a low-permeability clay bed. Its low shear strength is likely to be more susceptible to failure, hereby accelerating the erosion rate of an already fast-eroding sand basin. The resulting model can be used as input for locally constraining the ground parameters in coastal recession and erosion models.

KEYWORDS
coastal erosion, coastal monitoring, electrical resistivity tomography (ERT), glacial deposits, ground penetrating radar (GPR), Norfolk coast

1 | INTRODUCTION

In Europe, more than 200 million people live in coastal regions (i.e. regions having either a sea border or having more than half of the population within 50 km of the sea; Collet & Engelbert, 2013). With climate change, global sea-level rise and anthropogenic adjustment, coastal systems and low-lying areas increasingly experience submergence, coastal flooding, and coastal erosion while public authorities are struggling to find solutions (Wong et al., 2014). Year after year, many buildings are lost to the sea and the population is forced to evacuate in light of increasing coastal flooding and land loss (Burden et al., 2020). Beyond the habitat loss and the increasing natural

2310 | wileyonlinelibrary.com/journal/esp

Earth Surf. Process. Landforms. 2022;47:2310–2324.

hazard, erosion can also have a strong environmental impact by exposing coastal landfills that could contaminate waters and disrupt coastal ecosystems (Brand & Spencer, 2019). Worldwide, in the absence of appropriate measures to protect coastal regions, it is estimated that sea-level rise will displace tens of millions of people in the coming decades (McLeman, 2018).

Historically, coastal adaptation measures consisted of the installation of hard defences (e.g. sea walls, revetments, groynes, or artificial reefs) designed to diminish wave attack and slow down the erosion by trapping washed-out sediments. However, these structures showed only short-term and local efficiency. They were not designed to counter an important global sea-level rise, and they led to counterproductive effects with down-drift sediment starvation and erosion (Clayton, 1989; Dickson et al., 2006; Granja & De Carvalho, 2000; Malherbe et al., 2013). Nowadays, more sustainable and climate-resilient measures are being developed and implemented in several countries (Pranzini et al., 2015). To be effective, these management plans must be based on a good understanding of coastal erosion systems and reliable estimates of the shoreline recession (Kettle, 2012).

The main drivers of coastal erosion are wave attack, shore profile, rock properties, and climate (Ashton et al., 2011). Their relative role and combined effects are not yet well understood (Hapke & Plant, 2010) and more work is required to develop reliable predictive models of shoreline recession (Wong et al., 2014). Designing cost-efficient methods to facilitate data acquisition and site characterization and monitoring is a challenge yet to be tackled.

Coastal cliffs (albeit comprising cliffs made of 'soft' rocks) are characterized by dynamically linked cliff retreat and shore platform erosion, notably through sudden mass-wasting processes (Collins & Sitar, 2008; Prémaillon et al., 2018; Rosser et al., 2013). Many coastal cliff recession models focus on the influence of marine drivers (Ashton et al., 2011; Dickson et al., 2006; Fitton et al., 2016; Inman et al., 2002; Limber et al., 2018), but some studies have also demonstrated that rates of cliff retreat vary greatly according to lithology (Del Río et al., 2009; Hapke & Plant, 2010), moisture content (Dietze et al., 2020), and discontinuities or décollement layers that favour mass-wasting processes (Le Cossec et al., 2011). The compilation of erosion studies at a global scale presented by Prémaillon et al. (2018) suggests that cliff retreat is most clearly governed by the lithological nature of the cliffs. They suggest that cliffs' resistance to erosion can be expressed by a simplified Hoek and Brown rock mass strength criterion (i.e. weak, medium, strong) that is merging lithological description and fracturing/weathering state of the rock (Hoek & Brown, 1997). However, due to insufficient knowledge about rock strength distribution, 3D rock models are often oversimplified (Limber et al., 2018). There is a need for a cost-efficient strategy to acquire rock properties data so these can be more systematically included in the cliff recession models.

The majority of subsurface investigations rely on *in-situ* testing such as cone penetration tests (CPTs) and the collection of rock samples for laboratory testing (Coe et al., 2018). They provide direct and quantitative measurements of the rock mechanical properties, but only sample local points and provide discrete data. Consequently, the broad distribution of the geotechnical properties must be approximated via geo-statistics based on these local measurements. The reliability of geostatistical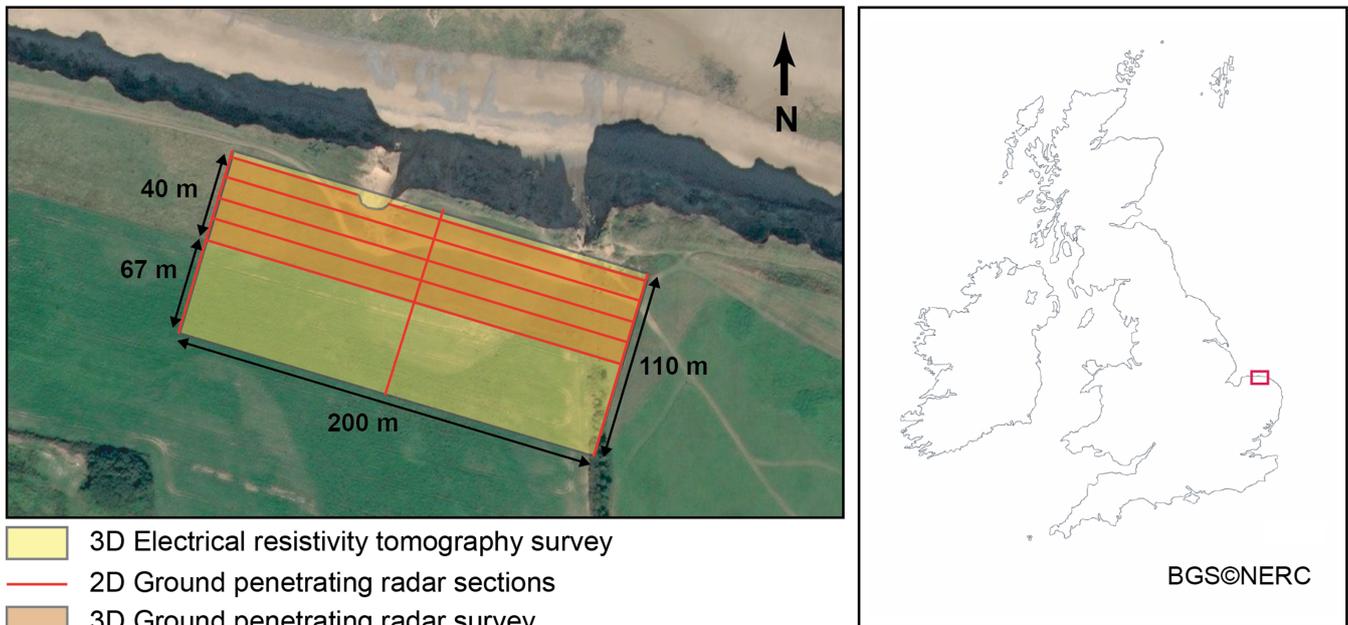 models is limited when the subsurface geology is complex, because of the high disparity of these properties. Further constraints to guide the statistical modelling in 3D are necessary.

In this study, we aim to characterize the cliff strength by acquiring volumetric geophysical data. Geophysical methods are non-destructive tools able to quickly measure geophysical properties within the subsurface. Constraining the geophysical data with ground-truth knowledge allows building 3D geological models of the subsurface. Furthermore, petrophysical property relationships allow translating geophysical data into 3D models of geotechnical and hydrological properties (Coe et al., 2018; Mayne et al., 2002). Previous studies have already used geophysical data to constrain the cliff properties, notably seismic methods to identify the basement rock (Inman et al., 2002), Bouguer gravity methods to identify aquifers on coastal cliffs (Jacob et al., 2018; Sajinkumar et al., 2017;), aerial electromagnetic methods to obtain large-scale ground resistivity distribution that can be correlated to unstable landslide areas (Nakazato & Konishi, 2005), or ground penetrating radar (GPR) methods to study paleo-events related to coastal hazards (Switzer et al., 2020). Here, we utilize high-resolution data to map the geology and water content of the subsurface by combining 3D electrical resistivity tomography (ERT) with multi-frequency GPR measurements, CPTs, and geological mapping along the shoreline. On the one hand, electrical resistivity can be used to determine *in-situ* rock properties and map the top of the water table and the soil salinity (Coe et al., 2018). On the other hand, GPR methods are sensitive to the electromagnetic properties of the soil. They provide complementary images, at a higher resolution than ERT, which help determine the stratigraphy in the shallow subsurface, locating fault zones, mapping the water table and the bedrock depth and saline interfaces (Jol & Bristow, 2003; Neal, 2004). Both methods are sensitive to the moisture and clay content (Goldman & Kafri, 2006; Huisman et al., 2003). An increased moisture or clay content leads to a reduction in the rock resistance, facilitating the triggering of landslides and more generally, coastal retreat (Dafalla, 2013; Yalcin, 2007). Laboratory studies have shown that reduced resistivity of granular material can be indicative of areas of low shear strength (Saarenketo & Scullion, 1996).

By combining 3D GPR and ERT data, this study aims to build a representative ground model that provides information regarding the soft sediment distribution, the presence of faults or décollement surfaces, and the relative moisture content distribution within the subsurface. The resulting ground model can be used as input to constrain the cliff strength spatial distribution. The study area is representative of many other coastal sites and the findings from this site can help understand coastal erosion at sites with similar geological settings. Furthermore, the methodological approach developed in this paper is applicable to other coastal sites of different geological settings where geophysical contrasts and properties allow the successful use of ERT and GPR.

2 | STUDY SITE LOCATION AND GEOLOGICAL SETTINGS

The study site is situated between West Runton and East Runton, northeast Norfolk coast, UK (Figure 1). It extends above a large glacitectonic sand basin that retreats at a higher rate than the adjacent till-dominated cliffs. In this area, coastal erosion of the

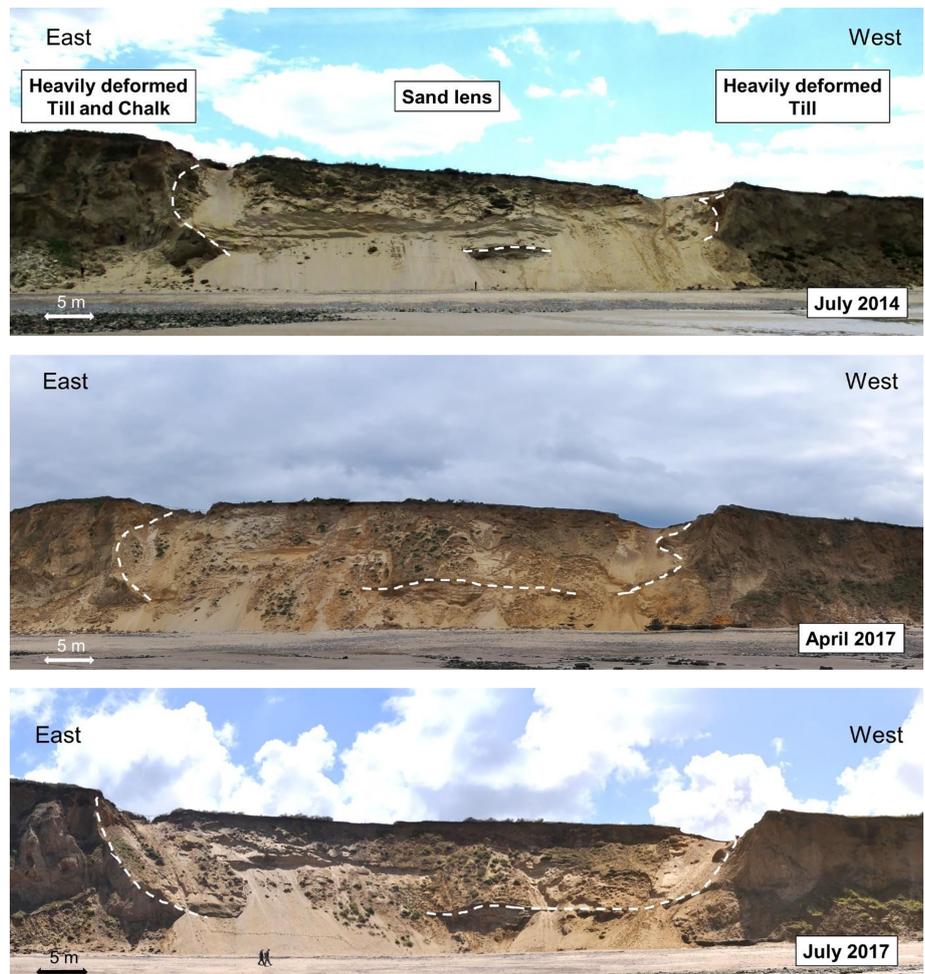**Indicative Erosion Zones Based on Current Policy Aims**

Indicative erosion zone up to 2025	Indicative erosion zone up to 2105
Indicative erosion zone up to 2055	Policy Unit boundary

FIGURE 1   Location of the study site compared with the indicative erosion zones and extent of the electrical resistivity tomography and ground penetrating radar surveys. The survey covers a sand basin well exposed on the shore's cliff to calibrate the geophysical models. The current models assume a relatively linear erosion trend parallel to the coast, which does not illustrate the locally higher erosion at the sand lens (modified from AECOM Limited, 2010). Imagery map from Esri, DigitalGlobe, GeoEye, Earthstar Geographics, CNES/Airbus DS, USDA, USGS, AeroGRID, IGN, and the GIS User Community (https://services.arcgisonline.com/ArcGIS/rest/services/World_Imagery/MapServer) [Color figure can be viewed at wileyonlinelibrary.com]

undefended cliffs can be averaged to −0.9 m/yr over the last 20 years (Environment Agency, 2013). The subsurface geology is clearly observable in the cliff section, providing a unique opportunity to link geophysical measurements with direct geological observations (Figure 2). It is a representative example of many glacitectonic sand basins, which are common along this part of the coastline.

FIGURE 2 Photograph of the cliff outcrop taken from the beach at three different times between 2014 and 2017. The limits of the sand lens are outlined with white dashes. Erosion affects mainly the softer sandy sediments within the lens, while other glacial tills are more resistant. By comparing the differences between July 2014 and April 2017, and between April 2017 and July 2017, one can see that the coastal retreat rate in 2017 was more important than within the previous three years [Color figure can be viewed at wileyonlinelibrary.com]

The regional Quaternary geology was most recently defined by Lee et al. (2017) as a complex glacigenic sequence comprising diamicton, glaciolacustrine sands and muds, and glaciofluvial outwash deposits. They record the successive episodes of ice marginal advance and retreat across the region that occurred during the Anglian Glaciation, 450 000 years ago (Figure 3). In total, six major ice advances (A1 to A6) have been described in East Anglia (Lee et al., 2017). In the study area, four glaciogenic units have been recognized (Phillips et al., 2008; Carr et al., 2016). From the base upwards, they comprise the Happisburgh Diamicton Member (HTM; associated with the A1 ice advance), the Bacton Green Diamicton Member (BGTM; associated with the A4 ice advance), the West Runton Mélange Member (WRM; associated with the A5 ice advance), and the Runton Sand and Gravel Member (RSGM; associated with the A5 ice advance). They overlie Upper Cretaceous Chalk bedrock, which crops out on the foreshore beneath the high-water mark, and the overlying Early to Middle Pleistocene shallow marine and coastal deposits of the Wroxham Crag Formation (WCF).

At the study site and extending westwards, these materials have been remobilized and largely intermixed, forming a glacitectonic mélange (the WRM). The mélange incorporates large rafts of remobilized chalk bedrock and the development of large glacitectonic sand basins (infilled by the RSGM) that formed contemporaneously along structurally defined thrust-tip ridges interpreted as thrust moraines (Phillips et al., 2008). This deformation occurred during the A5 advance (Lee et al., 2017).

Previous investigations along the North Norfolk coast concluded that erosion occurred largely through mass wasting (Dickson et al., 2006; Lee, 2008), when the strength of the cliff materials cannot support the stresses imposed by gravity and by the waves. In their numerical model, Dickson et al. (2006) attributed a single value of material strength to represent all areas of till cliff, thereby neglecting the variability in material strength. The Quaternary glacial deposits that compose the Norfolk cliffs are, however, very heterogeneous in nature and probably play an important role in the erosion variability along the coast. They consist of layers of permeable sand, gravels, low-permeability clays, and diamicton that locally result in zones of low shear strength prone to erosion and failure (Frew, 2009). The ponding of percolating water along low-permeability geological structures, where the porewater pressure builds up, further reduces the shear strength and creates slip surfaces prone to mass wasting (Lee et al., 2011). The mapping of the lithology and of these slip surfaces is therefore a valuable input for coastal erosion models.

So far, studies in North Norfolk have been mainly limited to 2D cross-sections along the outcrops, primarily along the shore. From those results, understanding the character and processes by which these sequences form and how the geological features (notably possible décollement surfaces) are evolving inland is difficult because information is available in one direction only (Lee, 2008).
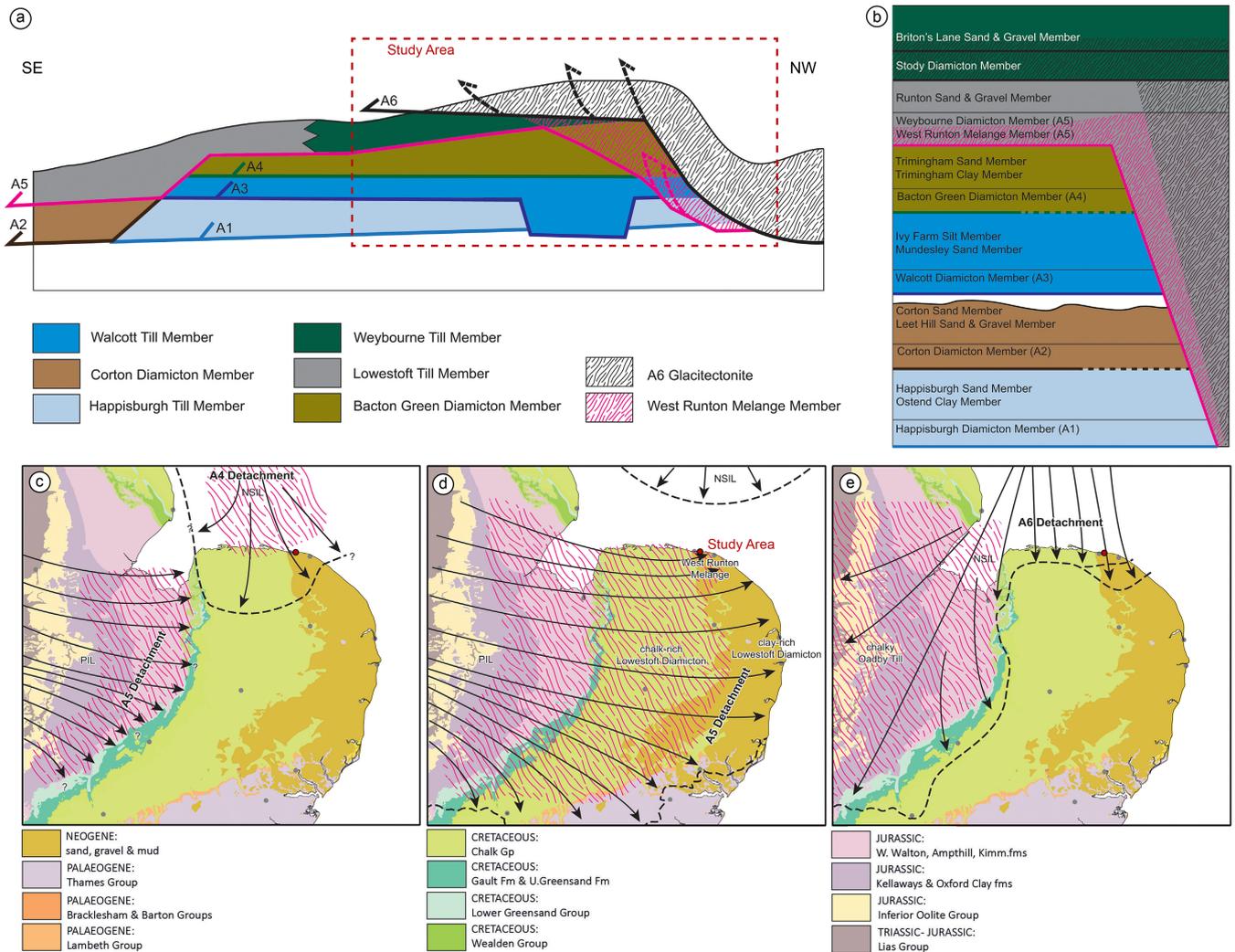
FIGURE 3 Overview of the geological settings of the study area (modified from Lee et al., 2017). (a) Hybrid stratigraphic model for northern East Anglia. (b) Simplified formation-level stratigraphic succession for northern East Anglia showing bounding A1–A6 detachments and major geological units. (c–e) Schematic palaeogeographical maps showing the glacial history of northern East Anglia and adjoining areas relative to: (c) the A4 and A5 detachments with the accretion of the Bacton Green Diamicton member in North Norfolk; (d) the main A5 detachment with subglacial deforming bed processes, development of terminal moraine–extensional basin complex, and accretion of the WRM in Northeast Norfolk; and (e) the detachment A6 with ice-marginal thrust-stacking and outwash sedimentation relative to a dynamic and oscillating margin in North Norfolk. NSIL: North Sea Ice Lobe [Color figure can be viewed at wileyonlinelibrary.com]

3 | MATERIALS AND METHODS

Previous studies have proven that GPR is an efficient method for mapping 3D glacitectonic structures and for investigating the lithology and depositional settings of glacial sediments (Bakker & Van Der Meer, 2003; Busby & Merritt, 1999; Fallon, 2012; Lønne et al., 2001; Overgaard & Jakobsen, 2001; Sadura et al., 2006; Wells, 2007). GPR was successfully used to image the inland extension of glacitectonic structures in North Norfolk between Sheringham and West Runton, but mainly using 2D common offset GPR (Carr et al., 2016). The maximum depth of penetration ranged between ~24 and 6 m with 25 and 100 MHz antennas, respectively. Results demonstrated that the combination of three survey frequencies (25, 50, 100 MHz antennas) was required to enable identification and interpretation of glacial deposits. Isolated 2D GPR profiles may be contaminated by out-of-plane reflections and may not be sufficient for imaging highly heterogeneous structures (McClymont et al., 2008). In contrast, 3D GPR data can provide high-resolution images of structures in any direction with

approximately equal fidelity, facilitating the prediction of sediment distribution. 3D geophysical data are therefore considered more appropriate for understanding the processes that control the distribution of the glacial deposits in the North Norfolk coast.

3D ERT and topographic data from an unmanned aerial vehicle (UAV) were acquired in 2015. The 3D ERT survey comprised 11 parallel acquisition lines, with 8 m line spacing and 4 m electrode spacing along those lines. Data were acquired using a dipole–dipole array, which has been shown to provide superior resolution of subsurface features compared to Wenner or Schlumberger arrays (Chambers et al., 2002). The survey comprised measurements with dipole length (a) of 4, 8, 12, 16, 20, and 24 m, and dipole spacings (n) of 1 to 8a, and a complete set of reciprocal measurements for error analysis and data weighting in the inversion (Tso et al., 2017). The measured resistances were inverted using E4D (Johnson et al., 2010) with an L2 norm on the model misfit to gain a 3D model of the subsurface resistivity distribution. Overlapping photography from the UAV was processed using the structure from motion (SfM) technique to derive

orthographic imagery, 3D point clouds, and ultimately a digital surface model. The photography was geocoded using a series of ground control points that were referenced using real-time kinematic (RTK) GPS. The UAV digital surface model was filtered and smoothed to produce the 3D topography of the studied cliff section that was then used to build the surface and subsurface discretization for the ERT inversion. Prior to inversion, data were filtered based on their reciprocal errors (removing all data with reciprocal errors above 10%). Measured reciprocal errors were used as data weights in the inversion under the condition that they were above a lower limit of 10% of the average reciprocal error level, which was calculated based on the errors between the 10th and 90th percentiles (Uhlemann et al., 2017). A forward modelling error of 2% of the measured resistance was added to the reciprocal error. The inversion converged to a chi-squared misfit criterion of one, meaning that the model fits well the data within their errors. After convergence, the root-mean-squared misfit is equal to 2.4%, which is interpreted to represent the data noise.

100 MHz 3D GPR data and low-frequency (50 and 25 MHz) 2D data were acquired in 2017. The survey parameters were based on Annan (2003) and adjusted based on the field conditions to avoid aliasing and ensure a dense inline sampling. The survey parameters are summarized in Table 1. All data were acquired with a perpendicular broadside configuration of the antennas. The 100 MHz 3D survey grid was set up based on the pre-existing corner points from the ERT survey that covered a 200 m × 90 m area (Figure 1). Inline data were recorded parallel to the coastline, perpendicular to the a-priori trend of the features under investigation (NNE–SSW oriented structures). Common offset GPR survey data were acquired with GPS control using a Sensors & Software pulseEKKO Pro system. The antennas were mounted on a rough terrain smart-cart, with a GPS antenna positioned at the centre between the two GPR antennas, 0.88 m above the ground. Each GPR trace was associated with a GPR record by the central unit, with a GPS record on average every eight traces (40 cm). In addition to the GPR points recorded during the acquisition, RTK GPS points were also measured using a Leica Viva GS15 antenna at a coarser interval to calibrate the results of the 3D grid and position the 2D lines.

Three different source frequencies were used to obtain data of different resolution and signal penetration: the lower frequencies aimed at imaging the base of the sand lens and the general architecture, while the higher frequencies were recorded to image the internal stratigraphy of the sand basin at higher resolution. Additionally, common midpoint (CMP) lines were acquired in both the inline and crossline direction to estimate and monitor the wave velocity, with values ranging between 0.1 and 0.12 m/ns. Based on this velocity, the maximum penetration depths were estimated to be around 16, 10, and 2 m for the 25, 50, and 100 MHz antennas, respectively.

Datasets were processed using ReflexW (v.8.1) and Matlab. GPS data were processed to correct for mis-positioning, altitude correction, and coordinate system conversion (see Figure S1 in the online Supplementary Information). To correct for the altitude anomalies of the GPS points and to generate a regular positioning grid, a topographic surface was interpolated based on the RTK GPS records. The GPR traces were then assigned to the new set of regular GPS points. The surveys of the different frequencies were processed following a common processing workflow designed to remove noise and bad traces, correct for acquisition settings, and compensate for signal attenuation before migration and depth conversion (see Figure S1).

Velocity models used for migration and depth conversion were based on the velocity analysis of CMP surveys and diffraction hyperbola analysis. CMP data could not be acquired at perfectly horizontal dipping layers and have been recorded only at three different points. To calibrate the velocity, shallow CPT using a Panda dynamic cone penetrometer have been performed to test soils' cone resistance. It could only reach a depth of 4.5 m from the surface, thus the calibration could not be performed in the deeper part of the profiles (Figure 4). The cone resistance can be related to the undrained shear strength and thus can be an indicator of the subsurface lithology (Langton, 1999). In this study, we approximate the relation between cone resistance and lithology without corrections. The measured data were filtered to remove anomalous measurements. The rapid increase in cone resistance from ∼7–10 MPa to ∼15–20 MPa is interpreted as the boundary between the soft sand and the hard tills. The low cone resistance at the intersection between the two is interpreted as a weak shear strength local plane, which is evidenced on the radar profile as the boundary surface between the two lithological units.

An average interval velocity of 0.13 m/ns for the sand lens and 0.1 m/ns for the till have been retained. The best migration results were obtained using a finite-difference scheme with a 15° approximation method. It should be noted that this migration scheme has

TABLE 1 Overview of the GPR acquisition parameters

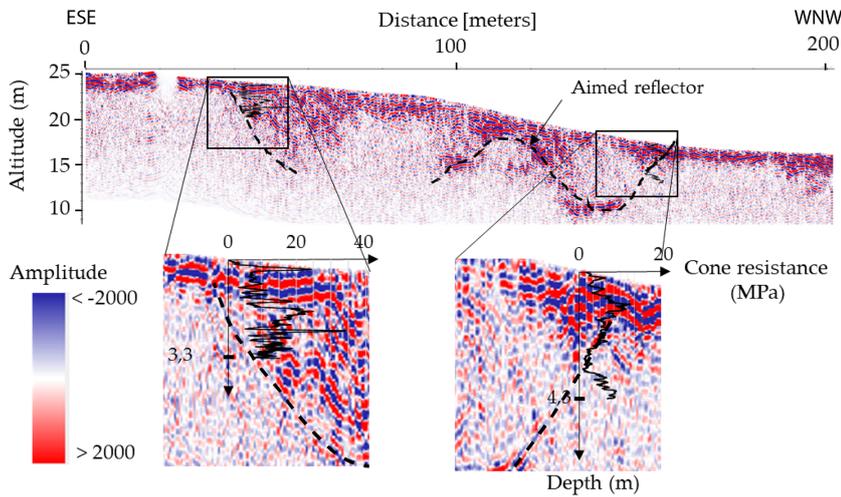| System	PulseEkko pro	PulseEkko pro	PulseEkko pro
Voltage (V)	90	400	400
Operating frequency (MHz)	100	50	25
Antennas separation (m)	1	2	4
Recording	Continuous	Step	Step
Time window (ns)	500	700	1100
Sampling interval (ps)	800	1600	3200
Station spacing (m)	∼0.25	0.5	1
Stacks	32	16	16
X-line spacing (m)	0.5	10	/
Y-line spacing	5 to 10	/	/
Number of X-lines	88	5	2
Number of Y-lines	22	1	0

FIGURE 4 100 MHz GPR data inline (about 30 m inland from the cliff) after time migration and conversion from time to depth, with a measured cone resistance profile overlaid on it. The dashed line illustrates the base of the sand lens. Significant changes in cone resistance were interpreted either as the transition from gravel to sand within the loess or as the boundary between the soft sand and the hard tills and allowed to verify depth conversion results [Color figure can be viewed at wileyonlinelibrary.com]
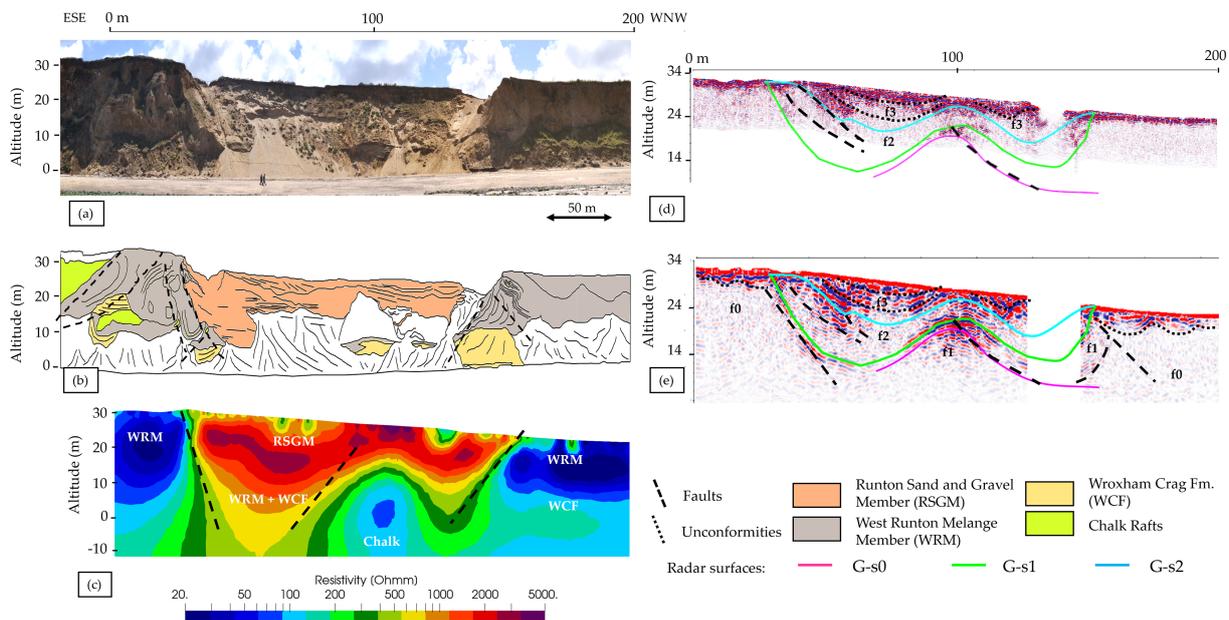

FIGURE 5 Comparison of the studied outcrop and the geophysical results: (a) photograph of the sand lens outcropping on the shore; (b) scheme of the outcrop showing the different lithological units interpreted based on previous studies of the Norfolk coast; (c) resistivity profile obtained from ERT data with the main lineation and the interpreted units overlaid on it; (d) 100 MHz X-line 00 (3 m inward from the cliff) radargram with the radar facies (f2 and f3) and the radar surfaces overlaid on it; (e) 50 MHz X-line 00 radargram with the main radar facies (f0, f1, f2, f3) and the radar surfaces overlaid on it. The geometry of the sand lens partially visible on the outcrop is clear on the geophysical data. The shape of the lens is comparable on ERT and GPR data, but the thickness of the lens differs. GPR data allow us to distinguish the internal architecture of the lens in 3D. Reflections outside the basin delimited by G-s1 could be assimilated to radar facies f3 but are not observed on the outcrop, thus they are assimilated to the hosting and radar facies f1 [Color figure can be viewed at wileyonlinelibrary.com]

limitations in handling steep reflections. After processing, the 100 MHz 3D dataset reached a vertical resolution of 30 cm in the shallowest part of the profiles, while the other frequencies have a resolution inferior to 1 m (1–1.3 m for the 50 MHz survey, 1.25–1.6 m for the 25 MHz survey).

4 | RESULTS

4.1 | Outcrop study

Three distinctive lithofacies assemblages were identified on the cliff outcrop (Figure 5):

- The WCF, consisting of grey interbedded gravels, sands, silts, and clays, with a weathered black bed at its lower part.
- Overlying the WCF, the WRM is a heterogeneous mixture of intermixed clay and sand-rich diamictons (HTM and BGTM) with thin and discontinuous layers of silt, clay, and pods of sand (WCF), and rafts of chalk bedrock. In the west part of the section, it mostly comprises thrusted and folded grey marly silts, with a small raft of chalk. The WRM is intermixed with the WCF and forms an anticlinoform on which the overlying basin's sediments overlap. At the eastern edge of the basin, it dips vertically, with 'till-prisms' of mixed diamicton that rest uncomfortably above the WCF.
- The RSGM, comprising well-sorted light yellow to yellow sands and silts, which coarsen upward with small occasional lenses of
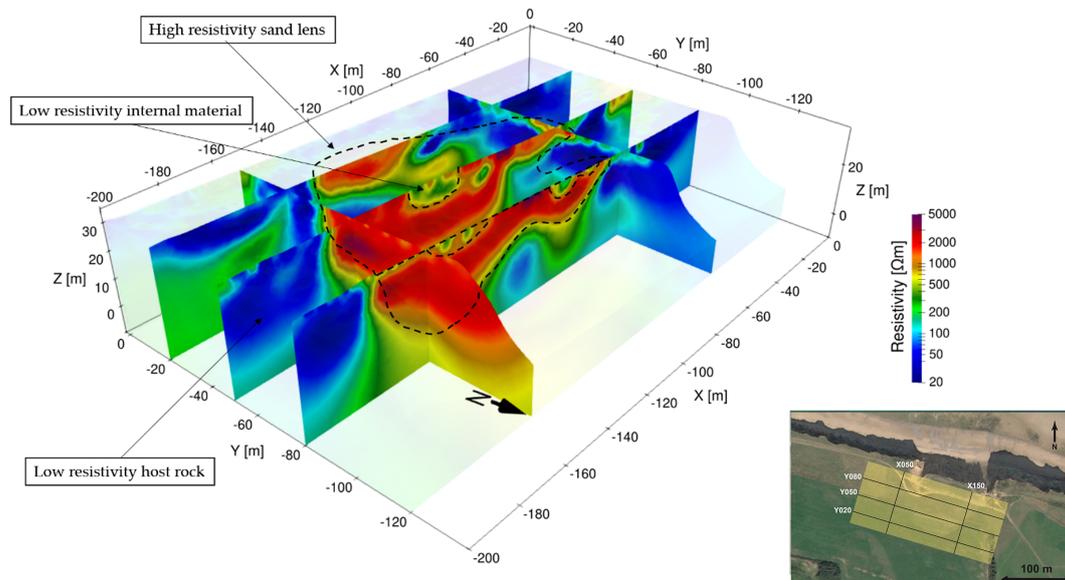
FIGURE 6   Resistivity model obtained from the 3D dipole–dipole ERT survey acquired in 2014. The highly resistive feature (outlined by the dotted lines following a 1000 Ωm isosurface) is interpreted as a wedge-shaped sand lens, embedded within a more conductive host rock (below 50–200 Ωm) interpreted as glacial tills. The sand-lens appears to be divided in two sub-basins, with zones of lower resistivity at their centres [Color figure can be viewed at wileyonlinelibrary.com]

gravel and clay. The bedding appears sub-horizontal but steepens slightly towards the edge of the basin and the anticlinoform, supporting the view that the infill of these basins occurred syn-tectonically (Phillips et al., 2008). The limits of the sand basin are marked by glacitectonic boundaries, with the WRM formed by sharp sub-vertical faults to the east and west. The bottom of the basin is marked by an erosive surface that cuts through the underlying sedimentary sequence.

4.2 | ERT

Preliminary analysis of the ERT data (Figure 6) revealed the presence of a highly resistive body (>1000 Ωm), interpreted as the sand lens, located within a significantly more conductive host material (10–200 Ωm). The sand lens appears wedge-shaped, 150 m wide by 90 m long, with a sharp sub-horizontal edge on the eastern side. It is oriented in a NE–SW direction, comprising what appear to be two sub-basins that intersect the cliff. They steadily thin towards the west and the south. The fine-scaled architecture of the sediments within the lens, notably the bedding, is not resolved in the ERT models, and prevents identifying potential faults within them. The employed smoothness constraints and the nature of the method also imply a decreasing resolution with increasing distance to the electrodes (i.e. depth). Hence, the exact location of the lower boundary of the sand basin cannot be accurately imaged.

4.3 | GPR

The interpretation of GPR data followed the scheme defined by Neal (2004) to describe radar surfaces, radar facies, and radar packages. Radar packages, facies, and surfaces are defined based on the differences in patterns, continuity, and strength of reflections on the

100 and 50 MHz datasets. Three radar packages, four radar facies, and three radar surfaces have been defined (Figure 5). The interpreted radar surfaces match well with the formation boundaries observed in the cliff.

The radar facies and the corresponding formations are summarized in Table 2. From the oldest to the youngest, they comprise:

- f0, a reflection-free facies, with low-resistivity material (below 50 Ωm). It fits with the position of the WRM on the side of the basin, where it is predominantly clayey (hence the higher attenuation and lower resistivity), reducing the depth of penetration (Jol & Bristow, 2003). It forms radar package RP-1, associated with the deformed rock hosting the sand basin.

- f1, a low-amplitude, low-continuity reflections facies, with numerous overlapping diffractions. The boundary G-s0 is a horizontal low-amplitude, non-continuous, large-wavelength reflector dipping towards the west at an angle of 23°. Radar facies f1 is truncated at the top by the radar surface G-s1, which is marked by a convex strong-amplitude reflection and matches well with the iso-resistivity surface at 1000 Ωm (Figure 6). This facies displays varying resistivity decreasing downward from 1000 to 100 Ωm. It is assimilated to the ridge at the centre of the basin, which appears to be made of WRM and WCF on the outcrop, underlain by either WCF or chalk. It forms a complex, highly deformed radar package RP-2 found beneath the ridge.

- f2, a sub-parallel, low to high-amplitude, moderately continuous reflections facies, locally deformed by several easterly dipping thrust faults, onlapping the underlying radar surface G-s1. Reflections are dipping towards the centre of the lowest points in the basin and show a top-lap condition with the overlying G-s2 radar surface. Radar surface G-s2 seems to fit with a change in the dips that is seen in the outcrop. At the vicinity of the ridge made of radar facies f1, it is of high amplitude and high wavelength while at the centre of the basin this facies is poorly imaged because of the strong attenuation of the radar signal. Facies f2 is associated with

TABLE 2 Interpreted relationship between the lithofacies identified on the outcrop, the radar facies, the radargrams, and the resistivity values on resistivity profiles inverted from ERT

Formation	Dominant lithofacies	Radar package	Radar facies	Resistivity (Ωm)
Runton Sand and Gravel	Stratified silts, sands, and unsorted gravels, coarsening upward, with an erosive gravel base. Maximum thickness observed: 20 m. Poor clay content but locally high clay content within the boulder clay stripes in the uppermost 3 m	RP-3 Elongated trough shaped and folded package	f3 – concave, sub-horizontal, concave, parallel, high-amplitude reflections	200–1000
			f2 – folded parallel, medium to high amplitude and moderately continuous reflections, underlain by a strong, low-frequency reflector	2000 to >5000
West Runton Mélange	Highly deformed mélange comprising Happisburgh, Bacton Green Diamicton members, Wroxham Crag and occasional chalk rafts. Maximum thickness observed: 25 m. Highly unsorted, rich in clay	RP-2 Complex folded and thrusted unit, making up the central ridge splitting the sand basin in two	f1 – low to medium amplitude, short continuity reflections, with numerous overlapping diffractions, reflection-free on the edges of the basin, complex folded and thrusted geometry	100–1000
		RP-1 Hosting rock	f0 – reflection-free	10–50
Wroxham Crag Formation	Interbedded gravels, sands, silts, and clays, with a weathered black bed at its lower part. Maximum thickness observed: 10 m. Medium clay content	Below radar vertical resolution	Affiliated with f0–f1 Affiliated with f0	100–500 200–500
Chalk	White chalk with flint interbeds			

very high electrical resistivity (2000 to >5000 Ωm). Together with radar facies f3, it forms an elongated trough-shaped radar package RP-3, centralized around the anticlinoform feature formed by the radar facies f1, and pinches out further inland.

- f3, a continuous, concave parallel, high-amplitude, high-wavelength reflectors facies, onlapping the underlying radar surface G-s2. It comprises two units, separated by an unconformity that shows a variable thickness. f3 is related to medium to high resistivity between 200 and 1000 Ωm.

The radar facies identified are comparable to the facies described within different glacial deposits with comparable GPR methods (Jakobsen & Overgaard, 2002; Overgaard & Jakobsen, 2001). By comparison with these studies, radar facies f0 and f1 correspond to tectonized glaciofluvial and stiffer cohesive sediments (WRM and WCF), with folding and thrust planes, and characterized by diffraction tails of medium to large reflection strength. Radar facies f2 is comparable to their glaciofluvial sediments facies, here deposited syntectonically with the deformation of radar facies f1. Radar facies f3 equate to their later down-wash of sandy sediments.

5 | DISCUSSION

5.1 | Volume and geometry of the sand basin

The combination of GPR and ERT methods allows a better understanding of the 3D geometry of the glacitectonic sand basins that occur along the North Norfolk coast. So far, the 3D form of the 'till-prisms' and the RSGM-filled sub-basins remains unclear due to a lack of clear 3D spatial expression along the cliff outcrops. The GPR data imaged well the 3D structures, including demonstrating evidence for faulting and thrusting within the subsurface. The results suggest that the sand basin can be delimited by the radar surface G-s1, which matches relatively well the iso-resistivity surface at 1000 Ωm. It delimits an asymmetric bow-shaped basin, oriented NE–SW to W–E and bordered by two north to northwesterly dipping thrust fronts that separate the RSGM filling the basin from the WRM and WCF hosting it. Within the basin itself, sediments onlap a NW–SE aligned ridge made of WRM and WCF.

The two interpretations of the sand basin derived from GPR and ERT results (Figure 7), based on the radar surface G-s1 and the iso-resistivity at 1000 Ωm, respectively, have similar lateral extents but different thicknesses. GPR data suggest a maximum depth of 21 m, versus 30 m based on resistivity models. This difference could be explained by both the uncertainties in the velocity model for GPR data and the decreasing reliability of the resistivity model with depth. It has some implications for the volume estimation of the sand basin. Using the 3D topography derived from the UAV photogrammetry for the top surface, the volume of the sand basin could be estimated to 63 000 m^3 using the G-s1 horizon, versus 90 000 m^3 using the 1000 Ωm interface. These volumes are calculated on the same surface area of 6900 m^2 and do not consider the continuation of the sand basin towards the cliff, out of the surveyed area (acquisition could not be performed over private property). The discrepancy between the two estimates can be
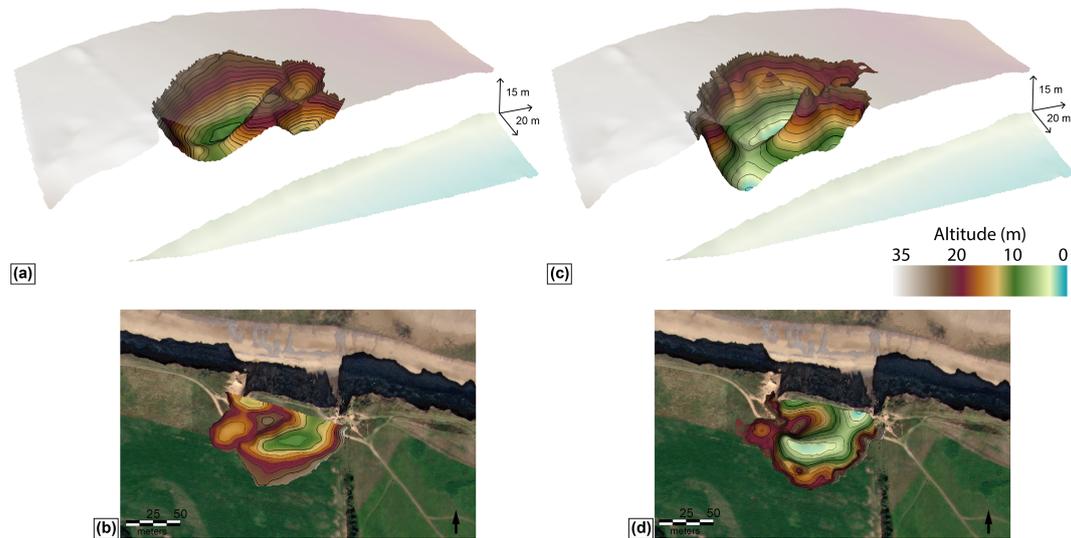
FIGURE 7 3D view and map view of the estimated base of the sand basin in the subsurface using two different geophysical methods. (a) 3D representation of the horizon picked on GPR data bounding the sand basin. (b) Depth map of the picked horizon bounding the sand basin with the main interpreted faults overlaid on it. (c) 3D representation of the maximum depth of iso-resistivity 1000 Ωm, interpreted as the bounding surface of the sand basin on ERT data. (d) Maximum depth map of the iso-resistivity 1000 Ωm [Color figure can be viewed at wileyonlinelibrary. com]

explained by the difference in resolution between the two geophysical methods.

For the GPR-based estimate, errors can be linked to the velocity model and the picking of the base of the sand basin. We estimate an approximate error of ±0.01 m/ns for the velocity of the sand basin on the limited CMP profiles. Uncertainties linked to picking of the base of the sand lens are due to the presence of clay-rich beds and 'pockets' that cause locally a rapid attenuation of the GPR signal, thereby decreasing the imaged depth at the centre of the basin. This translates into a variation of ±3 m for the maximum depth of the sand lens, resulting in a maximum thickness of 21 ± 3 m for the basin.

Concerning the ERT, inversion results are inherently non-unique, and an infinite number of solutions exist that explain the data equally well (Olayinka & Yaramanci, 2000). The sensitivity of geoelectrical measurements also decreases with depth, thus lowering the resolving capability of an array in the inversion of the data (Szalai et al., 2007). In our case, data were acquired along 200 m-long parallel transects, with a depth of investigation of approximately 30 m (Oldenburg & Li, 1999). This depth is close to the depth of the lower boundary of the sand lens, and hence interpreting the lower boundary of the sand lens is challenging. Finally, the smoothness constraints will cause even a sharp interface to be smooth. These factors make it difficult to determine an accurate depth of the sand lens from the ERT data.

By comparing the results with the outcrop, the depth estimated by the GPR data is considered more reliable than that estimated by the ERT. However, the ERT provides more insights on the geology beneath the sand lens (particularly at the shallower sections), where the GPR signal is strongly attenuated. Joint inversion of the ERT data using the GPR surfaces could help to characterize the geological features of interest and improve the 3D resistivity model of the investigated site. Studies by Doetsch et al. (2012) or Merz et al. (2015), for example, used GPR to image the 3D shape of the bedrock topography, and employ it as a 2D structural constraint for tomographic inversions of seismic and geoelectric data. A similar approach could also aid here to better define the depth of this deeper interface.

5.2 | Geological model

From the GPR results, the surface G-s0 identified below the sand basin is correlated with the main décollement surface that forms the base of the glacigenic sequence. This surface can be a kilometre to the west at West Runton according to Phillips et al. (2008), who described the décollement surface as a major stratigraphic boundary separating the older pre-glacial succession (WCF and chalk) from the younger glacial sediments (Figure 5). Above this décollement, steep-sided NE–SW to W–E oriented 'till-prisms' of WRM are identified on 3D models below the central ridge and at the flanks of the basin (Figure 8). The orientation of the 'till-prisms' supports the model of Phillips et al. (2008), where they describe sand-filled sub-basins tectonically bounded by the 'till-prisms' of WRM that developed along proglacial to subglacial thrust fronts (see their Figure 11) during the A5 ice advance.

The bow-shaped structure of the basin observed in 3D, with a bending of the basins from NE to W (Figure 7), and the dip of the sand infill towards the NE observed on GPR sections (Figure 8), suggests a second episode of deformation that distorted the shape of the pre-existing basin. In particular, the ridge at the centre of the sand basin appears as a WNW–ESE oriented anticlinoform structure made of WCF and WRM. Based on nearby outcrop studies, they were interpreted by Phillips et al. (2008) as NE–SW thrust faults apparently dipping towards the west and affiliated with the A5 advance. However, when observed in 3D, layers within the anticlinoform exhibit a north/northwest-oriented dip, with reflections parallel to the faults, and stop abruptly 20 m inland, relaying another northerly dipping unit (Figure 8). The same north/northwest-dipping structure is observed in the resistivity data, highlighted by the presence of a zone of low resistivity within the high-resistivity basin. ERT results also display an eastern-dipping lineament, which can be observed as deep as the current sea level, where resistive structures (100–500 Ωm) have been assimilated into the chalk. They are oriented in the opposite direction from the NE–SW to W–E thrust
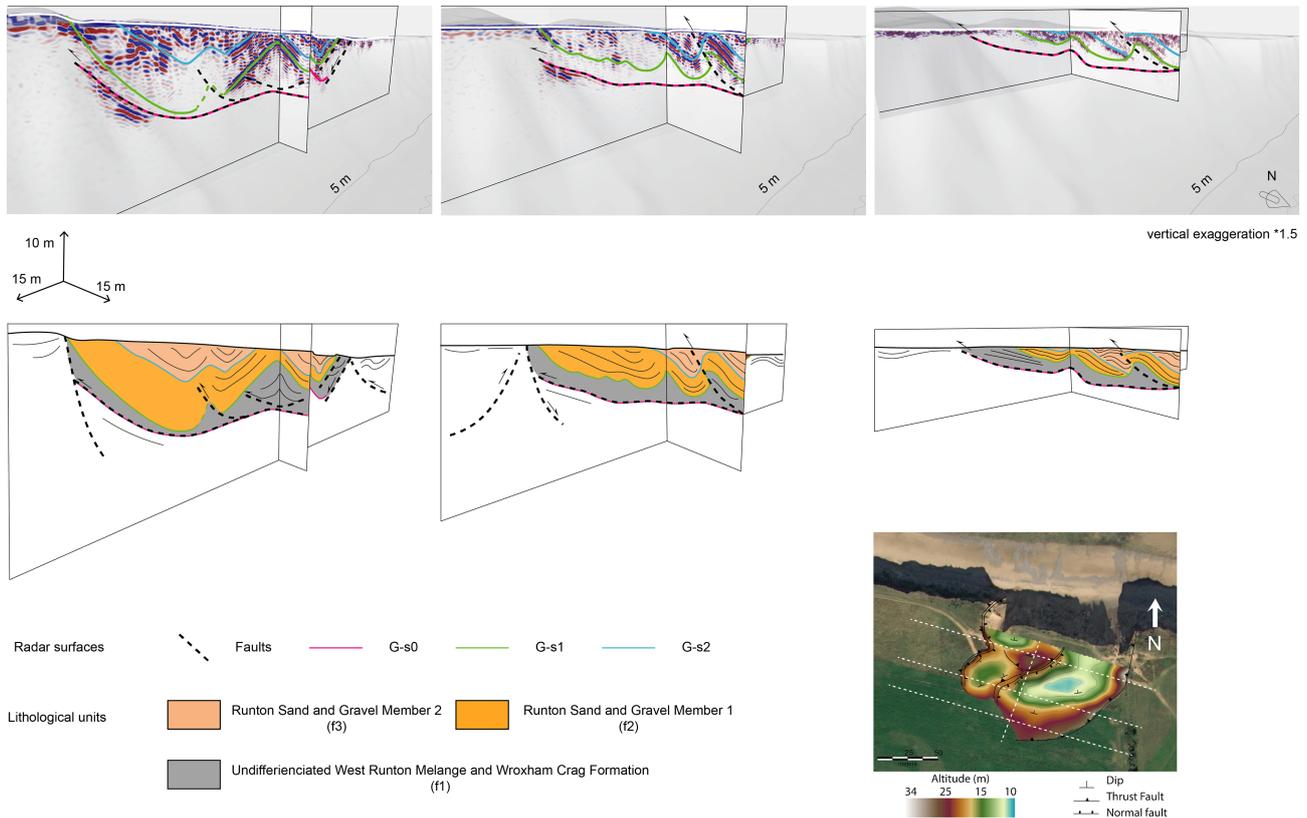
FIGURE 8 Geological model of the sand basin. (a) 3D scene of GPR profiles along the UAV cliff model (in transparent shades of grey), with the interpreted horizon (G-s0 to G-s3) and the lithological units interpreted on 50 MHz data (i, ii) and 100 MHz data (iii). (b) Interpreted 3D GPR scene across the sand basin showing the two directions of thrust, one west to northwest-dipping thrust front related to the A5 ice advance and one northern-dipping thrust front related to the A6 ice advance. (c) Smoothed depth map of G-s1 radar surface, with the location of the displayed GPR profiles. The strata within the sand basin dip towards the beach (i.e. towards the northeast) while they are considered to dip towards the west on the outcrop [Color figure can be viewed at wileyonlinelibrary.com]
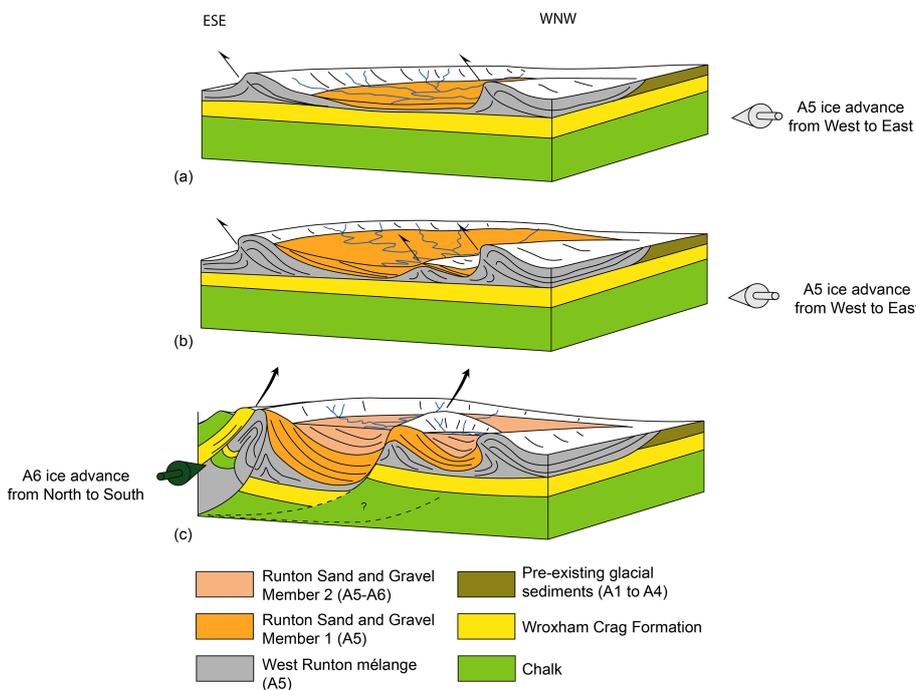

FIGURE 9 Tectonostratigraphic scheme of the geological model suggested for the sand basin. (a) Early A5 ice advance with accretion of the West Runton Mélange member formation and development of terminal moraine–extensional basin where the lower RSGM is deposited. (b) Mid to late A5 ice advance; the shortening increases and is accommodated with the initiation of a third thrust front within the terminal moraine–extensional basin. (c) A6 ice advance with the emplacement of ice-marginal northerly dipping thrust duplex, tilting of the sand lens, and outwash sedimentation of the upper RSGM [Color figure can be viewed at wileyonlinelibrary. com]

faults assimilated into the eastward A5 ice advance interpreted on the outcrop and on GPR data.

Based on the WNW–ESE orientation of this anticlinoform and the northeastern-dipping décollement, we suggest a second episode

of deformation due to a NE–SW compression related to a later A6 advance coming from the north/northwest (Figure 9c). This last advance has been recorded in Norfolk by E–W and NE–SW aligned thrust fronts that notably build up the Cromer ridge structure,

including several steep-sided ice contact hills that occur along the North Norfolk coast (Lee et al., 2017).

In a previous study, Burke et al. (2009) proposed an imbricated thrust stack model for the formation of a large complex of glacitectonic bedrock rafts at East Runton (approximately 1 km to the east of the study site), implying northerly dipping thrust branches formed during the later A6 ice advance. The two northerly dipping décollement surfaces observed on the data from the present study area show the same configuration as thrust structures observed at East Runton. The penetration depth does not identify whether chalk could be present beneath this ridge, but contrasts in resistivity seem to indicate so. Another argument supporting the imprint of the A6-related deformation is the change in dip between the radar facies f2 and f3 within the sand lens. Radar facies appear to be broadly parallel to the underlying structures, suggesting they were deposited before the generation of the anticlinoform created by the eastward A5 thrusting (Figure 9a), and then deformed with the hosting mélange (Figure 9b). By contrast, the sedimentary pattern of radar facies f3 indicates a discharge flow parallel to the ridge, exhibiting a similar 'bow-shaped' pattern. This suggests that radar facies f3 was deposited while the ridge was already present in the leading syncline created at the front of the thrust front but was then folded and imbricated into the duplex as the shortening from the A6 deformation event occurred (Figure 9c).

The geological model proposed here is valid for syntectonic basins formed in a proglacial setting. In this case, an initial phase of deformation (A5) was later followed by a second deformation event (A6) that occurred in an ice-marginal to subglacial setting. Based on the current knowledge of glacitectonic structures, this geological model is relevant to the glacitectonic sand basins that occur between East Runton and Weybourne to the west of Sheringham (Phillips et al., 2008; Phillips & Lee, 2013).

5.3 | Constraining erosion rates in space through geophysical methods

The lithology is likely to be the main driver of the high erosion rate of this sand body. Results from the CPT show that the RSGM is characterized by a low cone resistance, related to the relatively weak shear strength of the sand. Our results show that these sand basins prone to erosion can be easily mapped in 3D using ERT methods, where the sand is characterized by a high resistivity (above 1000 Ωm). But the high rate of erosion is also linked to the presence of low-permeability surfaces that dip towards the beach, highlighted by the radar surfaces G-s1 and Gs-2 on GPR results. These surfaces are outlined by a strong low-frequency reflector before a sudden loss of GPR signal, particularly at the centre of the basin, and a high-resistivity contrast around 1000 Ωm (Figure 5).

The strong attenuation of the radar signal along these surfaces could be related to a high clay or moisture content or a strong signal scattering. The presence of lacustrine marls at the centre of some of the sand basins has been reported by Phillips et al. (2008), thus favouring the presence of clay-rich low-permeability surfaces. Such impermeable beds could cause ponding of the percolating water along these surfaces. The low-resistivity anomaly observed in the upper RSGM seems to confirm this hypothesis. The resistivity

of the upper RSGM goes down to 100 Ωm, far below the expected resistivity for dry gravel and sands, which usually range between 500 and 10 000 Ωm (Palacky, 1987). This low anomaly can be linked to a high moisture content within the upper RSGM. An increased moisture content generates a higher pore pressure, which in turn increases the shear stress along these surfaces (Souisa et al., 2015). A high shear stress can facilitate slope failure processes. Even though the high erosion rate of these sand basins is primarily linked to their weak shear strength, the mass-wasting process, notably after heavy rains, could accelerate the erosion of these sand basins. Using geophysical methods, these low-permeability surfaces could be regionally mapped to better constrain erosion trends along the coast.

It should be noted that the current coastal protection plan intends to let these sand lenses erode naturally (AECOM Limited, 2010). This is because the eroded sand delivered from these basins to the beach is a finite sediment supply feeding the adjacent beaches. Consequently, their erosion seems more beneficial to coastal protection than their preservation.

5.4 | Limitations and perspectives

This study has tested the efficiency of ERT and GPR methods to investigate subsurface properties that can influence erosion.

ERT was able to clearly define the outline of the sand basin and its internal structure. It also provided information on the corresponding lithologies and likely water saturation. However, due to the inherent limitations of this technique, accurate imaging of the true depth of the features remains challenging. This limitation was addressed using GPR data, which imaged the interfaces at significantly higher resolution.

The use of 100 MHz antennas for investigating features of this type and anticipated geometry is not favoured. In this study, 100 MHz was chosen for both practical reasons (it was not possible to mount the 50 Hz antennas on the cart) and because of an incorrectly interpreted depth of the base of the basin during preliminary testing. The 3D GPR 100 MHz data failed in imaging the entirety of the sand basin. They provided the best resolution, but the weak depth of penetration only enabled the imaging of the uppermost units. The 3D GPR 100 MHz data could potentially reach the bottom of the shallow sub-basin made of facies f3 (the surface G-s2), which was clearly visible on depth-slices in the 3D volume, but the centre of the shallow basin could not be imaged due to the high attenuation. It also suffered from a low signal-to-noise ratio, which was difficult to compensate for during processing. The geometry of the sand basin was essentially defined with the 50 MHz data, but the resolution of this dataset is low (above 1 m), and only five 50 MHz GPR 2D sections were available. Isolated 2D GPR profiles may be contaminated by out-of-plane reflections and may not be sufficient for imaging highly heterogeneous structures (McClymont et al., 2008). Therefore, even though the results match well with ERT data, uncertainties remain regarding the exact geometry of the basin and its structural settings. Despite these drawbacks, 2D GPR sections have proven very useful for imaging the internal structures related to the basin's depositional history. They offer a resolution in depth which could not be reached with the ERT method.

For future investigations, acquiring 50 MHz 3D data or a dense 50 MHz 2D data grid could allow an improved assessment of the geometry of the basin and how it evolves over time during ongoing coastal erosion. Including the collection of CMP data throughout the study area, with an offset of at least 1.5 times the desired depth of investigation, is crucial to better constrain the migration and the time-to-depth conversion.

CONCLUSIONS

A representative cliff on the North Norfolk coast, UK, where erosion is controlled by the distribution of soft sediments and mass-wasting events, has been studied using a multidisciplinary approach combining 3D ERT, multi-frequency 3D and 2D GPR, geotechnical tests (CPT), and an outcrop study. Based on this example, we show that this approach allows building a detailed ground model of retreating coastal areas that can contribute to a better prediction of coastal recession.

ERT proved to be an efficient method to quickly delineate the basin and estimate the moisture content distribution within the subsurface. The mechanically soft sand basin is outlined by a 1000 Ωm isosurface with local wet and/or clay-rich zones of low resistivity within. This leads to a maximum thickness of 30 m and a volume of 89 807 m^3 of soft sediments to be eroded. The decrease in resolution with depth questions this result and the surfaces prone to mass wasting are not clearly identified.

3D and 2D GPR data have been acquired to further constrain the model. A more accurate base surface of the basin could be identified, revealing a maximum thickness of 21 ± 2 m, resulting in a volume of 63 040 m^3. The four interpreted radar facies (f0–f3) fit well with the resistivity distribution. Based on outcrop observation, these facies have been associated with geological formations. The GPR results show that the RSGM within the sand basin is strongly dipping towards the shore because of a post-sedimentary deformation linked to the A6 ice advance, where increased slope and shear stress favour mass wasting.

Interpretation of GPR and ERT data showed that the three identified radar surfaces (G-s0–G-s2) are characterized by an abrupt change in resistivity and a sudden high attenuation of the GPR-emitted waves that are associated with an increasing clay and/or water content. These surfaces appear impermeable enough to retain water, hence locally building up shear stress and reducing the shear strength, further increasing the risk of sand slides along these planes. GPR methods can be used to map these surfaces prone to mass events. The radar surfaces can also be used to structurally constrain the inversion of the ERT data and improve the accuracy of the estimated sand basin volumes.

ACKNOWLEDGEMENTS

CONFLICT OF INTEREST

The authors have no conflict of interest to declare.

DATA AVAILABILITY STATEMENT

The data that support the findings of this study are available from the corresponding author upon reasonable request.

ORCID

Simon Blondel https://orcid.org/0000-0001-8177-6676
Sebastian Uhlemann https://orcid.org/0000-0002-7673-7346
Arnaud Watlet https://orcid.org/0000-0003-0318-9032
Colm Jordan https://orcid.org/0000-0002-0624-6496
Jonathan Lee https://orcid.org/0000-0001-8610-2400

REFERENCES

AECOM Limited. (2010) *Kelling to Lowestoft Ness Shoreline Management Plan 6.* http://www.eacg.org.uk/docs/smp6/smp/kelling%20to%20lowestoft%20ness%20smp%20-%20final.pdf

Annan, A.P. (2003) *Ground Penetrating Radar: Principles, Procedures & Applications*. Mississauga, Ont.: Sensors & Software Inc.

Ashton, A.D., Walkden, M.J.A. & Dickson, M.E. (2011) Equilibrium responses of cliffed coasts to changes in the rate of sea level rise. *Marine Geology*, 284(1–4), 217–229. Available from: https://doi.org/10.1016/j.margeo.2011.01.007

Bakker, M.A. & Van Der Meer, J.J. (2003) Structure of a Pleistocene push moraine revealed by GPR: The Eastern Veluwe Ridge, The Netherlands. *Geological Society of London, Special Publications*, 211(1), 143–151. Available from: https://doi.org/10.1144/GSL.SP.2001.211.01.12

Brand, J.H. & Spencer, K.L. (2019) Potential contamination of the coastal zone by eroding historic landfills. *Marine Pollution Bulletin*, 146, 282–291. Available from: https://doi.org/10.1016/j.marpolbul.2019.06.017

Burden, A., Smeaton, C., Angus, S., Garbutt, A., Jones, L., Lewis, H. & Rees, S. (2020) Impacts of climate change on coastal habitats, relevant to the coastal and marine environment around the UK. Available at https://research-repository.st-andrews.ac.uk/handle/10023/19428 (accessed 7 June 2020).

Burke, H., Phillips, E., Lee, J.R. & Wilkinson, I.P. (2009) Imbricate thrust stack model for the formation of glaciotectonic rafts: An example from the Middle Pleistocene of North Norfolk, UK. *Boreas*, 38(3), 620–637. Available from: https://doi.org/10.1111/j.1502-3885.2009.00085.x

Busby, J. & Merritt, J. (1999) Quaternary deformation mapping with ground penetrating radar. *Journal of Applied Geophysics*, 41(1), 75–91. Available from: https://doi.org/10.1016/S0926-9851(98)00050-0

Carr, S., Ruiter, A., Nijhuis, M., Blacker, K. & Diggens, L. (2016) *A GPR Study of Glaciotectonic Structures at West Runton*. Norfolk: NERC Geophysical Equipment Facility Loan.

Chambers, J.E., Ogilvy, R. & Kuras, O. (2002) 3D electrical imaging of known targets at a controlled environmental test site. *Environmental Geology*, 41(6), 690–704. Available from: https://doi.org/10.1007/s00254-001-0452-4

Clayton, K.M. (1989) Sediment input from the Norfolk cliffs, Eastern England: A century of coast protection and its effect. *Journal of Coastal Research*, 5(3), 433–442.

Coe, J., Brandenberg, S., Ahdi, S. & Kordaji, A. (2018) *Geophysical Methods for Determining the Geotechnical Engineering Properties of Earth Materials*. Sacramento, CA: California Department of Transportation.

Collet, I. & Engelbert, A. (2013) Coastal regions: People living along the coastline, integration of NUTS 2010 and latest population grid. Available at https://ec.europa.eu/eurostat/web/products-statistics-in-focus/-/KS-SF-13-030?inheritRedirect=true [Accessed 7th June 2020].

Collins, B.D. & Sitar, N. (2008) Processes of coastal bluff erosion in weakly lithified sands, Pacifica, California, USA. *Geomorphology*, 97(3–4), 483–501. Available from: https://doi.org/10.1016/j.geomorph.2007.09.004

Dafalla, M.A. (2013) Effects of clay and moisture content on direct shear tests for clay–sand mixtures. *Advances in Materials Science and Engineering*, 2013, e562726. Available from: https://doi.org/10.1155/2013/562726

Del Río, L., Gracia, F. & Benavente, J. (2009) Mass movements and cliff retreat along the SW Spanish coast. *Journal of Coastal Research*, 56, 717–721.

Dickson, M., Walkden, M., Hall, J., Pearson, S. & Rees, J. (2006) Numerical modelling of potential climate-change impacts on rates of soft-cliff recession, Northeast Norfolk, UK. In *Proceedings of the 5th International Conference on Coastal Dynamics*. https://doi.org/10.1061/40855(214)34

Dietze, M., Cook, K.L., Illien, L., Rach, O., Puffpaff, S., Stodian, I. & Hovius, N. (2020) Impact of nested moisture cycles on coastal chalk cliff failure revealed by multiseasonal seismic and topographic surveys. *Journal of Geophysical Research: Earth Surface*, 125(8), e2019JF005487. Available from: https://doi.org/10.1029/2019JF005487

Doetsch, J., Linde, N., Pessognelli, M., Green, A.G. & Günther, T. (2012) Constraining 3-D electrical resistance tomography with GPR reflection data for improved aquifer characterization. *Journal of Applied Geophysics*, 78, 68–76. Available from: https://doi.org/10.1016/j.jappgeo.2011.04.008

Environment Agency. (2013) Coastal Trends Report – North East Norfolk and North Suffolk (Kelling Hard to Lowestoft Ness). Shoreline Management Group: Peterborough.

Fallon, N.K. (2012) Multi-frequency ground-penetrating radar (GPR) study of glaciofluvial outwash deposits, Limehouse, Ontario. PhD thesis, McMaster University, Hamilton, Ont.

Fitton, J.M., Hansom, J.D. & Rennie, A.F. (2016) A national coastal erosion susceptibility model for Scotland. *Ocean & Coastal Management*, 132, 80–89. Available from: https://doi.org/10.1016/j.ocecoaman.2016.08.018

Frew, P. (2009) An Introduction to the North Norfolk Coastal Environment. Coastal Management Unit NNDC. https://www.north-norfolk.gov.uk/media/3128/appendix_a__n_norfolk_coastal_environment.pdf

Goldman, M. & Kafri, U. (2006) Hydrogeophysical applications in coastal aquifers. In: Vereecken, H., Binley, A., Cassiani, G., Revil, A. & Titov, K. (Eds.) *Applied Hydrogeophysics*, NATO Science Series, Vol. 71. Dordrecht: Springer, pp. 233–254. https://doi.org/10.1007/978-1-4020-4912-5_8

Granja, H.M. & De Carvalho, G.S. (2000) Inland beach migration (beach erosion) and the coastal zone management (the experience of the northwest coastal zone of Portugal). *Periodicum Biologorum*, 102, 413–424.

Hapke, C. & Plant, N. (2010) Predicting coastal cliff erosion using a Bayesian probabilistic model. *Marine Geology*, 278(1–4), 140–149. Available from: https://doi.org/10.1016/j.margeo.2010.10.001

Hoek, E. & Brown, E.T. (1997) Practical estimates of rock mass strength. *International Journal of Rock Mechanics and Mining Sciences*, 34(8), 1165–1186. Available from: https://doi.org/10.1016/S1365-1609(97)80069-X

Huisman, J.A., Hubbard, S.S., Redman, J.D. & Annan, A.P. (2003) Measuring soil water content with ground penetrating radar: A review. *Vadose Zone Journal*, 2(4), 476–491. Available from: https://doi.org/10.2136/vzj2003.4760

Inman, D.L., Masters, P.M. & Jenkins, S.A. (2002) Facing the coastal challenge: Modeling coastal erosion in Southern California. Available at https://escholarship.org/uc/item/3kk9s8q9 [Accessed 23rd November 2020].

Jacob, T., Samyn, K., Bitri, A., Quesnel, F., Dewez, T., Pannet, P. & Meire, B. (2018) Mapping sand and clay-filled depressions on a coastal chalk clifftop using gravity and seismic tomography refraction for landslide hazard assessment, in Normandy, France. *Engineering Geology*, 246, 262–276. Available from: https://doi.org/10.1016/j.enggeo.2018.10.007

Jakobsen, P.R. & Overgaard, T. (2002) Georadar facies and glaciotectonic structures in ice marginal deposits, northwest Zealand, Denmark. *Quaternary Science Reviews*, 21(8–9), 917–927. Available from: https://doi.org/10.1016/S0277-3791(01)00045-2

Johnson, T.C., Versteeg, R.J., Ward, A., Day-Lewis, F.D. & Revil, A. (2010) Improved hydrogeophysical characterization and monitoring through parallel modeling and inversion of time-domain resistivity and induced-polarization data. *Geophysics*, 75(4), WA41. Available from: https://doi.org/10.1190/1.3475513

Jol, H.M. & Bristow, C.S. (2003) GPR in sediments: Advice on data collection, basic processing and interpretation, a good practice guide. *Geological Society of London, Special Publications*, 211(1), 9–27. Available from: https://doi.org/10.1144/GSL.SP.2001.211.01.02

Kettle, N.P. (2012) Exposing compounding uncertainties in sea level rise assessments. *Journal of Coastal Research*, 28, 161–173. Available from: https://doi.org/10.2112/JCOASTRES-D-10-00011.1

Langton, D. (1999) The Panda lightweight penetrometer for soil investigation and monitoring material compaction. *Ground Engineering*, 32, 33–37.

Le Cossec, J., Duperret, A., Vendeville, B.C. & Taibi, S. (2011) Numerical and physical modelling of coastal cliff retreat processes between La Hève and Antifer capes, Normandy (NW France). *Tectonophysics*, 510(1–2), 104–123. Available from: https://doi.org/10.1016/j.tecto.2011.06.021

Lee, E. (2008) Coastal cliff behaviour: Observations on the relationship between beach levels and recession rates. *Geomorphology*, 101(4), 558–571. Available from: https://doi.org/10.1016/j.geomorph.2008.02.010

Lee, J.R., Pennington, C.V.L. & Hobbs, P.R.N. (2011) Trimingham: Structural architecture of the Cromer Ridge Push Moraine complex and controls for landslide geohazards. In: Phillips, E., Lee, J.R. & Evans, H.M. (Eds.) *Glacitectonics: Field Guide*. London: Quaternary Research Association, pp. 218–227. http://qra.org.uk/publications/field_guides

Lee, J.R., Phillips, E., Rose, J. & Vaughan-Hirsch, D. (2017) The Middle Pleistocene glacial evolution of northern East Anglia, UK: A dynamic tectonostratigraphic–parasequence approach. *Journal of Quaternary Science*, 32(2), 231–260. Available from: https://doi.org/10.1002/jqs.2838

Limber, p.W., Barnard, P.L., Vitousek, S. & Erikson, L.H. (2018) A model ensemble for projecting multidecadal coastal cliff retreat during the 21st century. *Journal of Geophysical Research: Earth Surface*, 123(7), 1566–1589. Available from: https://doi.org/10.1029/2017JF004401

Lønne, I., Nemec, W., Blikra, L. & Lauritsen, T. (2001) Sedimentary architecture and dynamic stratigraphy of a marine ice-contact system. *Journal of Sedimentary Research*, 71(6), 922–943. Available from: https://doi.org/10.1306/030901710922

Malherbe, B., Fordeyn, A.J. & Defloor, B.D. (2013) Flanders bays on Belgian North Sea coast: Smart beach & dune nourishments to achieve an integrated and sustainable reinstatement of beach barrier systems. In *Proceedings of WODCON XX – Congress and Exhibition: The Art of Dredging*.

Mayne, P.W., Christopher, B.R. & Delong, J. (2002) *Subsurface Investigations – Geotechnical Site Characterization*. Washington, DC: US Department of Transportation, Federal Highway Administration.

McClymont, A.F., Green, A.G., Villamor, P., Horstmeyer, H., Grass, C. & Nobes, D.C. (2008) Characterization of the shallow structures of active fault zones using 3-D ground-penetrating radar data. *Journal of Geophysical Research: Solid Earth*, 113, B10315. Available from: https://doi.org/10.1029/2007JB005402

McLeman, R. (2018) Migration and displacement risks due to mean sea-level rise. *Bulletin of the Atomic Scientists*, 74(3), 148–154. Available from: https://doi.org/10.1080/00963402.2018.1461951

Merz, K., Maurer, H., Rabenstein, L., Buchli, T., Springman, S.M. & Zweifel, M. (2015) Multidisciplinary geophysical investigations over an alpine rock glacier. *Geophysics*, 81(1), 147157. Available from: https://doi.org/10.1190/geo2015-0157.1

Nakazato, H. & Konishi, N. (2005) Subsurface structure exploration of wide landslide area by aerial electromagnetic exploration. *Landslides*, 2(2), 165–169. Available from: https://doi.org/10.1007/s10346-005-0056-2

Neal, A. (2004) Ground-penetrating radar and its use in sedimentology: Principles, problems and progress. *Earth-Science Reviews*, 66(3–4),

261–330. Available from: https://doi.org/10.1016/j.earscirev.2004.01.004

Olayinka, A.I. & Yaramanci, U. (2000) Assessment of the reliability of 2D inversion of apparent resistivity data. *Geophysical Prospecting*, 48(2), 293–316. Available from: https://doi.org/10.1046/j.1365-2478.2000.00173.x

Oldenburg, D.W. & Li, Y. (1999) Estimating depth of investigation in dc resistivity and IP surveys. *Geophysics*, 64(2), 403–416. Available from: https://doi.org/10.1190/1.1444545

Overgaard, T. & Jakobsen, p.R. (2001) Mapping of glaciotectonic deformation in an ice marginal environment with ground penetrating radar. *Journal of Applied Geophysics*, 47(3–4), 191–197. Available from: https://doi.org/10.1016/S0926-9851(01)00064-7

Palacky, G.J. (1987) Resistivity characteristics of geologic targets. In: Nabighian, M.N. (Ed.) *Electromagnetic Methods in Applied Geophysics*, Vol. 1. Houston, TX: Society of Exploration Geophysicists, pp. 53–129.

Phillips, E. & Lee, J.R. (2013) Development of a subglacial drainage system and its effect on glacitectonism within the polydeformed Middle Pleistocene (Anglian) glacigenic sequence of North Norfolk, Eastern England. *Proceedings of the Geologists' Association*, 124(5), 855–875. Available from: https://doi.org/10.1016/j.pgeola.2012.07.005

Phillips, E., Lee, J.R. & Burke, H. (2008) Progressive proglacial to subglacial deformation and syntectonic sedimentation at the margins of the Mid-Pleistocene British Ice Sheet: Evidence from North Norfolk, UK. *Quaternary Science Reviews*, 27(19–20), 1848–1871. Available from: https://doi.org/10.1016/j.quascirev.2008.06.011

Pranzini, E., Wetzel, L. & Williams, A.T. (2015) Aspects of coastal erosion and protection in Europe. *Journal of Coastal Conservation*, 19(4), 445–459. Available from: https://doi.org/10.1007/s11852-015-0399-3

Prémaillon, M., Regard, V., Dewez, T.J.B. & Auda, Y. (2018) GlobR2C2 (Global Recession Rates of Coastal Cliffs): a global relational database to investigate coastal rocky cliff erosion rate variations. *Earth Surface Dynamics Discussions*, 6, 651–668, Available from: https://doi.org/10.5194/esurf-6-651-2018

Rosser, N.J., Brain, M.J., Petley, D.N., Lim, M. & Norman, E.C. (2013) Coastline retreat via progressive failure of rocky coastal cliffs. *Geology*, 41(8), 939–942. Available from: https://doi.org/10.1130/G34371.1

Saarenketo, T. & Scullion, T. (1996) *Using Electrical Properties to Classify the Strength Properties of Base Course Aggregates*. College Station, TX: Texas Transportation Institute.

Sadura, S., Martini, I., Endres, A. & Wolf, K. (2006) Morphology and GPR stratigraphy of a frontal part of an end moraine of the Laurentide Ice Sheet. *Geomorphology*, 75(1–2), 212–225. Available from: https://doi.org/10.1016/j.geomorph.2005.01.014

Sajinkumar, K.S., Kannan, J.P., Indu, G.K., Muraleedharan, C. & Rani, V.R. (2017) A composite fall-slippage model for cliff recession in the sedimentary coastal cliffs. *Geoscience Frontiers*, 8(4), 903–914. Available from: https://doi.org/10.1016/j.gsf.2016.08.006

Souisa, M., Hendrajaya, L. & Handayani, G. (2015) Determination of landslide slip surface using geo-electrical resistivity method at Ambon City Moluccas-Indonesia. *International Journal of Emerging Technology and Advanced Engineering*, 5, 42–47.

Switzer, A., Gouramanis, C., Bristow, C. & Simms, A. (2020) Ground-penetrating radar (GPR) in coastal hazard studies. In: Engel, M., Pilarczyk, J., May, S.M., Brill, D. & Garrett, E. (Eds.) *Geological Records of Tsunamis and Other Extreme Waves*. Amsterdam: Elsevier, pp. 143–168.

Szalai, S., Novák, A. & Szarka, L. (2007) Depth of investigation of dipole–dipole, noncolinear and focused geoelectric arrays. In *Proceedings of the 13th European Meeting of Environmental and Engineering Geophysics*, Istanbul, Turkey, 3–5 September.

Tso, C.M., Kuras, O., Wilkinson, P.B., Uhlemann, S., Chambers, J.E., Meldrum, P.I., et al. (2017) Improved characterisation and modelling of measurement errors in electrical resistivity tomography (ERT) surveys. *Journal of Applied Geophysics*, 146, 103–119. Available from: https://doi.org/10.1016/j.jappgeo.2017.09.009

Uhlemann, S., Chambers, J., Wilkinson, P., Maurer, H., Merritt, A., Meldrum, P., et al. (2017) Four-dimensional imaging of moisture dynamics during landslide reactivation. *Journal of Geophysical Research: Earth Surface*, 122(1), 398–418. Available from: https://doi.org/10.1002/2016JF003983

Wells, C.M. (2007) *Investigating Coarse-Grained Glacio-Fluvial Outwash with Ground Penetrating Radar (GPR), Harpursville Susquehanna Valley, New York*. Binghamton, NY: State University of New York at Binghamton.

Wong, P.P., Losada, I.J., Gattuso, J.-P., Hinkel, J., Khattabi, A., McInnes, K., et al. (2014) Coastal systems and low-lying areas. In Climate Change 2014: Impacts, Adaptation, and Vulnerability. Part A: Global and Sectoral Aspects. Contribution of Working Group II to the Fifth Assessment Report of the Intergovernmental Panel on Climate Change. Cambridge University Press: Cambridge; 361–409.

Yalcin, A. (2007) The effects of clay on landslides: A case study. *Applied Clay Science*, 38(1–2), 77–85. Available from: https://doi.org/10.1016/j.clay.2007.01.007

SUPPORTING INFORMATION

Additional supporting information may be found in the online version of the article at the publisher's website.

How to cite this article: Blondel, S., Uhlemann, S., Inauen, C., Watlet, A., Maurer, H., Jordan, C. et al. (2022) Imaging mass-wasting sliding surfaces within complex glacial deposits along coastal cliffs using geophysics. *Earth Surface Processes and Landforms*, 47(9), 2310–2324. Available from: https://doi.org/10.1002/esp.5379